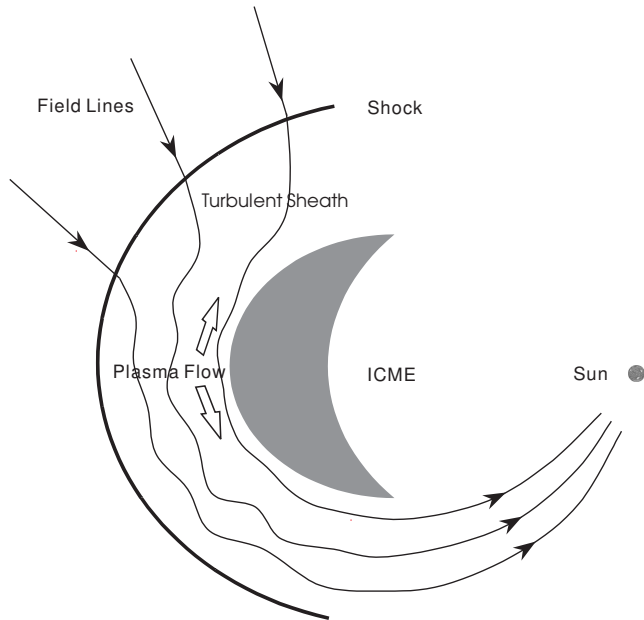


# Plasma Depletion and Mirror Waves Ahead of Interplanetary Coronal Mass Ejections

Y. Liu<sup>1</sup>, J. D. Richardson<sup>1</sup>, J. W. Belcher<sup>1</sup>, J. C. Kasper<sup>1</sup>, and R. M. Skoug<sup>2</sup>

**Abstract.** We find that the sheath regions between fast interplanetary coronal mass ejections (ICMEs) and their preceding shocks are often characterized by plasma depletion and mirror wave structures, analogous to planetary magnetosheaths. A case study of these signatures in the sheath of a magnetic cloud (MC) shows that a plasma depletion layer (PDL) coincides with magnetic field draping around the MC. In the same event, we observe an enhanced thermal anisotropy and plasma beta as well as anti-correlated density and magnetic fluctuations which are signatures of mirror mode waves. We perform a superposed epoch analysis of ACE and Wind plasma and magnetic field data from different classes of ICMEs to illuminate the general properties of these regions. For MCs preceded by shocks, the sheaths have a PDL with an average duration of 6 hours (corresponding to a spatial span of about 0.07 AU) and a proton temperature anisotropy  $\frac{T_{\perp p}}{T_{\parallel p}} \simeq 1.2 - 1.3$ , and are marginally unstable to the mirror instability. For ICMEs with preceding shocks which are not MCs, plasma depletion and mirror waves are also present but at a reduced level. ICMEs without shocks are not associated with these features. The differences between the three ICME categories imply that these features depend on the ICME geometry and the extent of upstream solar wind compression by the ICMEs. We discuss the implications of these features for a variety of crucial physical processes including magnetic reconnection, formation of magnetic holes and energetic particle modulation in the solar wind.



**Figure 1.** Schematic diagram of the turbulent sheath between an ICME and the preceding shock in the solar equatorial plane, illustrating the field line draping and consequent plasma flow.

## 1. Introduction

Plasma depletion layers (PDLs) and mirror mode waves are common features of planetary dayside magnetosheaths [e.g., Kaufmann et al., 1970; Crooker et al., 1979; Hammond et al., 1993; Violante et al., 1995; Hill et al., 1995]. The phys-

ical explanation for the plasma depletion is that the plasma is squeezed out of the local noon region as the magnetic field drapes around the magnetosphere [Zwan and Wolf, 1976]. Combining this model with the double-adiabatic equations derived by Chew et al. [1956], Crooker and Siscoe [1977] predict that a temperature anisotropy of  $T_{\perp} > T_{\parallel}$  is a direct consequence of the magnetic field line draping and plasma depletion, where  $\perp$  and  $\parallel$  denote the directions perpendicular and parallel to the magnetic field. When the temperature anisotropy exceeds the instability threshold, mirror mode waves are generated.

Magnetic field draping may occur in front of an obstacle in the solar wind if the magnetized plasma cannot penetrate the obstacle. Coronal mass ejections (CMEs), large-scale magnetic structures expelled from the Sun, form large obstacles called interplanetary coronal mass ejections (ICMEs) as they propagate into the solar wind. The ambient magnetic field may be draped around fast ICMEs, similar to the case of planetary magnetosheaths [Gosling and McComas, 1987; McComas et al., 1988]. Figure 1 shows an idealized sketch of this field line draping. An ICME with its axis lying in the solar equatorial plane creates a preceding shock if its speed relative to the ambient solar wind exceeds the fast-mode speed. Note that the ICME may still remain magnetically connected to the Sun. In front of the shock, the ambient magnetic field has the form of a Parker spiral. Between the shock and ICME is the sheath region where the magnetic field becomes stretched and turbulent. The shocked solar wind plasma is compressed in the direction perpendicular to the magnetic field, which may cause the plasma to flow along the draped field lines and result in formation of a PDL. The plasma temperature is enhanced in the perpendicular direction by the compression and depressed along the magnetic field by the parallel flow. As a result, anisotropic ion distributions are produced [e.g., Crooker and Siscoe, 1977]. When the threshold condition

$$\frac{T_{\perp p}}{T_{\parallel p}} - 1 > \frac{1}{\beta_{\perp p}} \quad (1)$$

is satisfied, the plasma is unstable to the mirror mode instability [Chandrasekhar et al., 1958]. The perpendicular plasma beta of protons is defined as  $\beta_{\perp p} = \frac{n_p k_B T_{\perp p}}{B^2/2\mu_0}$  with  $n_p$ ,  $k_B$ ,  $B$  and  $\mu_0$  representing the proton density, Boltzmann constant, magnetic field strength and permeability of free space, respectively. This picture should apply to ICMEs with any axis orientation. Therefore, PDLs and mirror mode waves are expected to form ahead of fast ICMEs. The presence and properties of these features may depend on the geometry of the ejecta and how much the magnetic field is draped and compressed. Unlike the case of planetary magnetosheaths, ICMEs expand in the solar wind and the spatial span of their sheath regions increases since the preceding shock usually moves faster than the ejecta.

A possible PDL lasting about 3 hours in front of an ICME was identified and investigated by Farrugia et al. [1997], based on an ideal magnetohydrodynamic (MHD) theory developed by Erkaev et al. [1995]. Mirror mode structures which appear to be ahead of an ICME were also found in the solar wind [Tsurutani et al., 1992]. In this paper, we use a case study and statistical analysis to investigate plasma depletion and mirror waves associated with ICMEs. Section 2 describes the observational data and data analysis. Section 3 shows an example of a PDL and mirror waves in the sheath region of an ICME. A superposed epoch analysis (SEA) of ICMEs, presented in section 4, gives evidence that these features are usually observed ahead of ICMEs preceded by shocks. We close by summarizing and discussing the results in section 5 and test the SEA in the Appendix. This paper provides the first consistent view of plasma depletion and mirror waves in the environment of ICMEs.

## 2. Observations and Data Reduction

We use solar wind plasma and magnetic field observations at 1 AU from ACE and Wind. Particularly important are the temperature anisotropy data which are needed to identify mirror mode waves. The ACE and Wind plasma teams use two different algorithms to calculate  $T_{\perp}$  and  $T_{\parallel}$ . The Wind team fits the measured ion velocity distributions with a convecting bi-Maxwellian function, using the magnetic field data to determine the parallel and perpendicular directions [e.g., Kasper et al., 2002]. The accuracy of their thermal anisotropies may be affected by angular fluctuations of the magnetic field; spectra with angular fluctuations over  $15^\circ$  are rejected. The ACE team calculates the second moment integrals of the measured distributions to obtain the temperature anisotropy. The resulting temperature matrix is then rotated into a field-aligned frame, which gives two perpendicular and one parallel temperature [e.g., Gary et al., 2001]. If the plasma is gyrotropic (i.e., particle gyration in a plane perpendicular to the magnetic field has no preferred direction), the two perpendicular temperatures should be the same; we only include the data for which the ratio of the two perpendicular temperatures is less than 1.3.

We use mainly ICMEs from the list of Liu et al. [2005] which are observed at both ACE and Wind. Events with  $T_p/T_{ex} \leq 0.5$  and  $n_{\alpha}/n_p \geq 8\%$  were qualified as ICMEs,

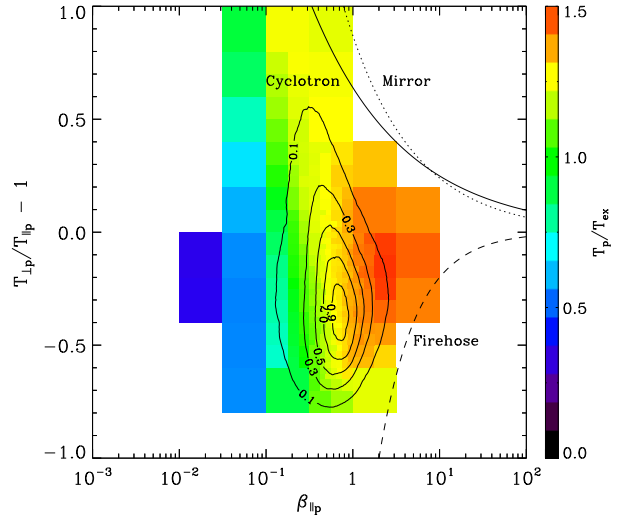


**Figure 2.** ACE measurements of the normalized proton temperature  $T_p/T_{ex}$  over the thermal anisotropy and parallel plasma beta of protons. The color shading indicates the average values of  $T_p/T_{ex}$  for the data binning. Black contours display the 2D histogram overlaid on the data at levels of [0.1, 0.3, 0.5, 0.7, 0.9]. Also shown are the thresholds for the firehose (dashed line), cyclotron (solid line) and mirror (dotted line) instabilities.

where  $T_p$ ,  $T_{ex}$  and  $n_{\alpha}$  are the proton temperature, expected proton temperature and alpha density separately. The expected temperature is calculated from the observed temperature-speed relationship at each spacecraft using the method of Lopez [1987]. We did not require the two criteria to be satisfied everywhere in an ICME interval. The boundaries of ICMEs are adjusted by incorporating other signatures of ICMEs [Neugebauer and Goldstein, 1997, and references therein]. A subset of ICMEs that have a strong magnetic field, smooth field rotation and low proton temperature are defined as magnetic clouds (MCs) [Burlaga et al., 1981]. The ICMEs are further sorted into three categories: MCs and ICMEs (non-MCs) with preceding shocks and ICMEs without preceding shocks. Events with large data gaps in the sheath region are rejected, which gives a total 18 MCs preceded by shocks, 21 ICMEs (non-MCs) with forward shocks and 56 ICMEs without shocks between 1998 and 2005. All the shocks upstream of the ICMEs are fast shocks across which the magnetic field strength increases. We note that although identification of ICMEs is a subjective art, the study of sheath regions by definition requires a preceding shock. Since almost all shocks inside 2 - 3 AU are generated by ICMEs, the uncertainties inherent in identifying ICMEs are not a major difficulty for this work.

We compare the thermal anisotropies determined from the Wind non-linear fittings to those obtained from the ACE moment integrals for different plasma regimes. Figure 2 shows ACE observations of the normalized temperature  $T_p/T_{ex}$  as a function of the temperature anisotropy and parallel plasma beta of protons. The parallel plasma beta of protons is defined as  $\beta_{\parallel p} = \frac{n_p k_B T_{\parallel p}}{B^2/2\mu_0}$ . A similar plot for Wind data can be found in Liu et al. [2006, Figure 9]. The  $1.7 \times 10^6$  ACE 64 s temperature averages from 1998 - 2005 are divided into two-dimensional bins of temperature anisotropy and plasma beta; bins with dense spectra are further subdivided, with the requirement that each cell contains at least 2000 data points. The curves indicate the

<sup>1</sup>Kavli Institute for Astrophysics and Space Research, Massachusetts Institute of Technology, Cambridge, MA, USA.

<sup>2</sup>Space Science and Applications, Los Alamos National Laboratory, Los Alamos, NM, USA.

threshold conditions

$$\frac{T_{\perp p}}{T_{\parallel p}} - 1 = \frac{S}{\beta_{\parallel p}^{\alpha}} \quad (2)$$

for the cyclotron, mirror and firehose instabilities, respectively. The free parameters,  $S$  and  $\alpha$ , are determined from solutions to the single-fluid MHD equations or to the Vlasov dispersion relation [Parker, 1958; Gary et al., 1997]. The firehose instability has  $S = -2$  and  $\alpha = 1$ , while  $S = 0.64$ ,  $\alpha = 0.41$  for the cyclotron instability over the range  $0.1 \leq \beta_{\parallel p} \leq 10$  and  $S = 0.87$ ,  $\alpha = 0.56$  for the mirror mode in the domain  $5 \leq \beta_{\parallel p} \leq 50$  at the maximum growth

rate  $\gamma_m = 0.01\Omega_p$ . Here  $\Omega_p$  denotes the proton cyclotron frequency. Most of the data are constrained by these thresholds; when the thermal anisotropy is close to the thresholds, the plasma is heated by the induced instabilities. As indicated by the contour lines, the most probable temperature anisotropy for the solar wind at 1 AU is  $T_{\perp p}/T_{\parallel p} = 0.6 - 0.7$ . This ratio can be increased in the sheath regions of fast ICMEs to 1.1 - 1.3. The ICME plasma, characterized by  $T_p/T_{ex} \leq 0.5$ , lies far away from the instability thresholds. These results are consistent with the picture described by Wind data [Liu et al., 2006]. We conclude that the two methods used to derive the thermal anisotropies give similar results.

### 3. Case Study

We first present a study of the association of a PDL and mirror mode waves with an ICME observed by ACE and Wind on April 16 - 17 (day 106 - 107), 1999. Figure 3 shows the ACE data, with the ICME interval indicated by the shaded area. The ICME was identified based on the enhanced helium/proton density ratio, declining speed, and depressed proton temperature; the smooth, strong magnetic field and large rotation of the  $B_y$  component (see Figure 5) indicate that this event is an MC. A forward shock driven by the event passed the spacecraft at 10:34 UT on April 16, with simultaneous sharp increases in the proton density, bulk speed, temperature and magnetic field strength. Within the sheath region, between the shock and the leading edge of the MC, the proton density first increases due to the compression at the shock and then decreases closer to the MC. This density decrease is the plasma depletion mentioned above. As shown by the bottom panel, fluctuations in the density and magnetic field strength are out of phase during the density increase; the correlation coefficient is about  $-0.6$  for the data subtracted by the backgrounds (refer to subsection 3.3) between 11:00 and 15:30 UT on April 16. The anti-correlation is also revealed by Figure 6

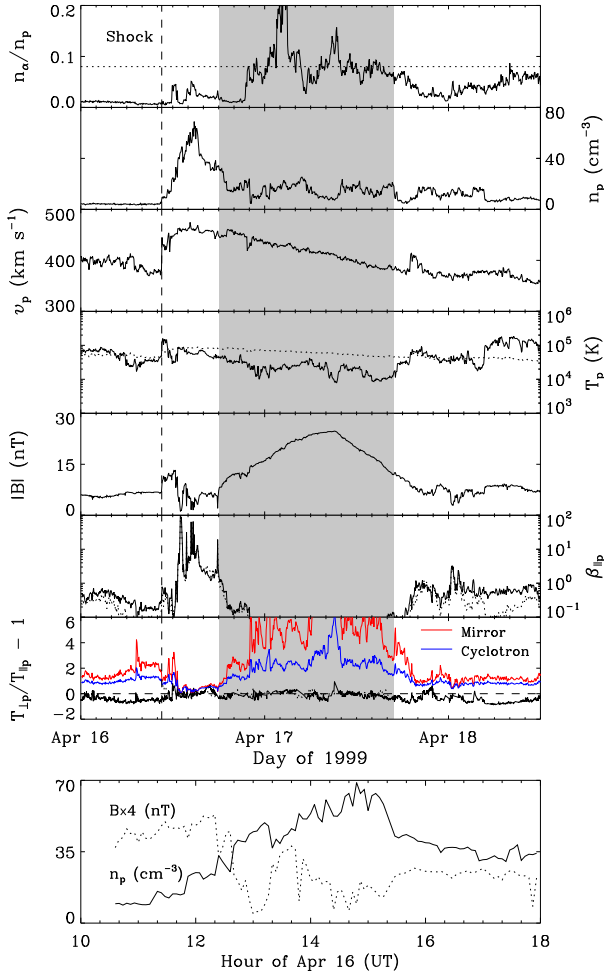


**Figure 3.** Solar wind plasma and magnetic field parameters measured by ACE for a 2.5-day interval in 1999. From top to bottom, the panels show the alpha-to-proton density ratio, proton density, bulk speed, proton temperature, magnetic field strength, parallel proton beta  $\beta_{\parallel p}$ , thermal anisotropy, and an expanded view of the magnetic and density fluctuations within the sheath. The shaded region shows an MC. Dashed lines indicate the arrival time of the MC-driven shock and the zero level of the anisotropy, respectively. Dotted lines denote the 8% level of the alpha/proton density ratio (top panel), the expected proton temperature (fourth panel), the perpendicular proton beta  $\beta_{\perp p}$  (sixth panel), and the scaled Wind data (seventh panel). Mirror and cyclotron thresholds (computed from ACE data) are shown by the colored lines.

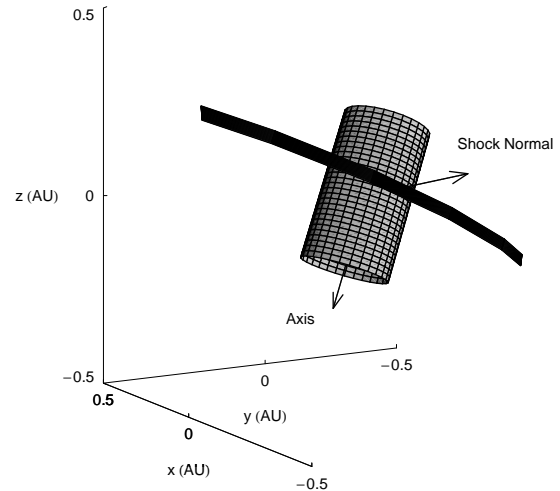


**Figure 4.** 3D rendering of the MC in GSE coordinates. Arrows indicate the axis orientation and shock normal, respectively. The belt around the flux tube approximates the shock surface.

combined with equations (3) and (5). This signature is typical for mirror waves. The second to last panel shows the temperature anisotropy and instability threshold conditions calculated from equation 2 for mirror and cyclotron instabilities. The dotted line in this panel shows Wind data scaled and time shifted to match the sheath and MC intervals seen at ACE. Anisotropies derived from Wind fit and ACE moment integrals are in agreement. The thermal anisotropy,  $\frac{T_{\perp p}}{T_{\parallel p}} - 1$ , is near zero inside the MC but drops to  $\sim -0.4$  in the ambient solar wind. In the sheath region, the anisotropy is as high as 0.5 (exceeding the instability thresholds) and has an average value of 0.2 - 0.3 (very close to the thresholds). The plasma beta (its effect is also reflected by the instability thresholds) is very high in the sheath after 12:29 UT on April 16, with values sometimes exceeding 50. As is evident from Figure 2, the mirror threshold is lower than the cyclotron limit when  $\beta_{\parallel p} > 6$ , which is also indicated in Figure 3. Therefore, mirror instabilities are excited in the sheath and give rise to the anti-correlated density and magnetic field fluctuations. More evidence is provided below for the plasma depletion and mirror mode structures.

### 3.1. Flux-rope and Shock Orientation

The mechanism described in section 1 for generation of PDLs and mirror mode waves may fit these observations. To test this fit requires knowledge of the MC and shock orientation. Minimum variance analysis (MVA) [Sonnerup and Cahill, 1967] provides estimates of the MC axis orientation using the measured magnetic field vectors [e.g., Lepping et al., 1990; Bothmer and Schwenn, 1998]. Eigenvectors of the magnetic variance matrix,  $\hat{\mathbf{y}}^*$ ,  $\hat{\mathbf{z}}^*$ ,  $\hat{\mathbf{x}}^*$ , corresponding to the eigenvalues in descending order, form a right-handed orthogonal coordinate system. MCs are oriented along the intermediate variance direction ( $\hat{\mathbf{z}}^*$ ). Application of the MVA method to the normalized magnetic field measurements within the MC gives an axis, in terms of the azimuthal ( $\theta$ ) and longitudinal ( $\phi$ ) angles, of  $\theta = -69^\circ$  and  $\phi = 91^\circ$  in the geocentric solar ecliptic (GSE) coordinates. We also determine the axis orientation with a flux-rope reconstruction technique, based on the Grad-Shafranov equation [Hau and Sonnerup, 1999; Hu and Sonnerup, 2002]; the resulting axis orientation is very close to the MVA estimate.

Figure 4 is a 3D view of the MC modeled as a cylindrical flux rope with a diameter of 0.23 AU (obtained from the average speed multiplied by the MC duration in Figure 3) in the GSE system. Note that the x axis points from the Earth to the Sun, so the Sun lies at (1, 0, 0) AU in the system. The flux rope is viewed from (-2, 1.5, 0) AU relative to the origin (Earth) of the system and is almost perpendicular to the ecliptic plane. The dark belt around the MC represents part of the shock surface which is approximated as a sphere centered at the Sun. The distance between the shock and the MC is about 0.08 AU along the ACE trajectory. The upper arrow points in the direction of the shock normal with  $\theta = 7^\circ$  and  $\phi = 178^\circ$  determined from a least-squares fit to the Rankine-Hugoniot relations [Viñas and Scudder, 1986]. Magnetic coplanarity gives a comparable result using the average magnetic field vectors upstream and downstream of the shock. The angle between the shock normal and upstream magnetic field is about  $61^\circ$ , so the shock is oblique. The shock normal makes an angle of about  $96^\circ$  with the flux-rope axis. Therefore, the whole situation can be pictured as a flux rope nearly perpendicular to the ecliptic plane moving away from the Sun (along the -x direction) and driving an oblique shock ahead of it. In the MC frame, the ambient field lines may be draped around the MC, analogous to planetary magnetosheaths.

The shock speed can be calculated from  $v_s = \frac{n_2 v_2 - n_1 v_1}{n_2 - n_1}$  given by the conservation of mass across the shock. Substituting the upstream density  $n_1 = 4 \text{ cm}^{-3}$  and velocity  $v_1 = 375 \text{ km s}^{-1}$  and the downstream  $n_2 = 9 \text{ cm}^{-3}$  and  $v_2 =$

$430 \text{ km s}^{-1}$ , we obtain  $v_s \simeq 474 \text{ km s}^{-1}$ , slightly larger than the MC leading-edge speed of  $450 \text{ km s}^{-1}$ . The size of the sheath, between the MC and shock, is thus expected to increase with distance. The MC is also expanding in the solar wind, as shown by the speed difference between the leading and trailing edges (see Figure 3). These two factors may affect the formation of PDLs and anisotropic ion distributions within the sheath.

### 3.2. Plasma Depletion and Magnetic Field Draping

Figure 5 provides an expanded view of the PDL and shows that it is associated with field line draping. The dashed lines bracket the PDL, in which the proton density decreases by a factor of 2 within 2.6 hours. Within the MC the  $B_y$  component, not  $B_z$  as usually seen in MCs, exhibits a large rotation, which confirms our MC axis determination. Interestingly, the magnetic field is nearly radial inside this PDL as indicated by the comparison of the  $B_x$  component with the field strength. Note that the spiral magnetic field makes an angle of  $45^\circ$  with the radial direction on average near the Earth; a radial field seldom occurs. The bottom panel shows the dot product of the field direction with the axis orientation, which is typically near zero in the PDL, so the field lines in the PDL are perpendicular to the MC axis. This product reaches its maximum close to the MC center. In contrast, the dot product between the field direction and the minimum variance direction ( $\hat{\mathbf{x}}^*$ ) of the MC magnetic field is almost -1 in the PDL but roughly constant throughout the MC interval. The configurations of the flux rope

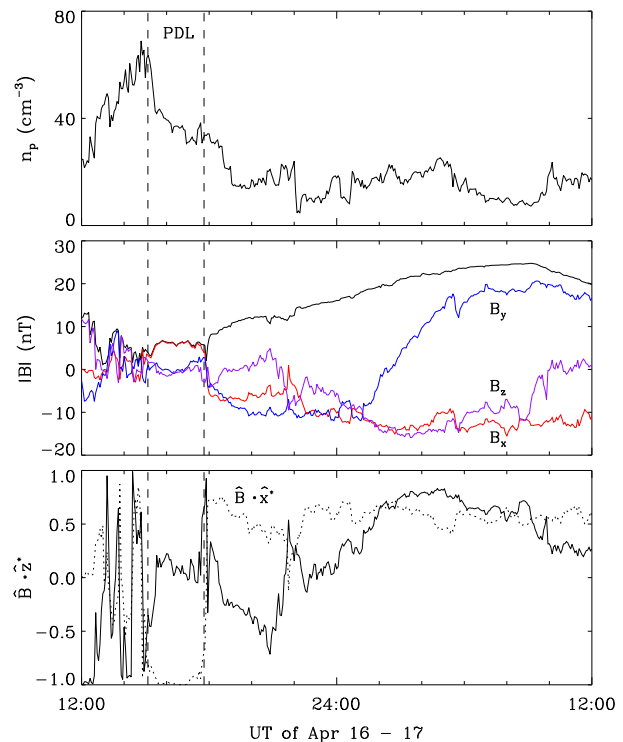


**Figure 5.** Proton density (upper panel), magnetic field magnitude with its components denoted by the colored lines (middle panel), and the dot product of the field direction with the MC axis orientation (lower panel) encompassing the PDL between the vertical dashed lines. The dotted line in the bottom panel shows the dot product between the field direction and the minimum variance direction of the MC magnetic field.



and field lines within the PDL give direct evidence for field line draping. The good time coincidence between the density decrease and field line draping strengthens confidence for these features.

### 3.3. Wave Structures

Mirror mode instabilities produce anti-correlated density and magnetic field fluctuations, namely,

$$\frac{\delta n}{n} = -\left(\frac{T_{\perp}}{T_{\parallel}} - 1\right) \frac{\delta B}{B} \quad (3)$$

for a bi-Maxwellian plasma [e.g., Hasegawa, 1969], where  $\delta n$  and  $\delta B$  are perturbations in the background plasma density  $n$  and magnetic field strength  $B$ . However, in the same low frequency regime the slow mode, alone among the three basic MHD modes, also has a plasma density variation out of phase with the magnetic field fluctuation. Starting with the CGL theory [Chew et al., 1956], we obtain the relationship between density and magnetic field fluctuations

$$\frac{\delta n}{n} = \left(\frac{P_{\perp} \sin^2 \theta}{nm_p}\right)^{-1} \left[ \frac{\omega^2}{k^2} - \frac{B^2}{\mu_0 nm_p} - \frac{P_{\perp}}{nm_p} + \frac{P_{\parallel} \cos^2 \theta}{nm_p} \right] \frac{\delta B}{B}, \quad (4)$$

where  $m_p$  is the proton mass,  $\theta$  is the angle between the wave vector  $\mathbf{k}$  and the magnetic field, and  $P_{\perp}$ ,  $P_{\parallel}$  are the perpendicular and parallel thermal pressures. The dispersion relation,  $\frac{\omega^2}{k^2}$ , is given by Parks [2004, equation (9.247), see the errata]. Equation (4) is a general relationship between the density and magnetic fluctuations for the slow and fast modes. It can be shown from equation (4) that the fast mode always gives positively correlated  $\delta n$  and  $\delta B$ . The firehose instability arising from this mode will also induce in-phase density and magnetic field fluctuations, at least in its linear stage. The intermediate mode with a dispersion relation  $\frac{\omega^2}{k^2} = v_A^2 \left( \frac{P_{\perp} - P_{\parallel}}{B^2/\mu_0} + 1 \right) \cos^2 \theta$  is not involved with the perturbations so that  $\delta n = \delta B = 0$  across this mode as in the ordinary MHD theory. Here  $v_A$  denotes the Alfvén speed.

The direction of the wave vector can be estimated using MVA on the measured magnetic field. For plane waves, the propagation vector lies along the minimum variance direction. The best estimate of the direction is roughly normal to the magnetic field with an average value of  $93^\circ$  for the interval with active fluctuations in the sheath region, so the waves may be highly oblique. Therefore, equation (4) can be reduced to

$$\frac{\delta n}{n} = -\left(1 + \frac{2}{\beta_{\perp}}\right) \frac{\delta B}{B} \quad (5)$$

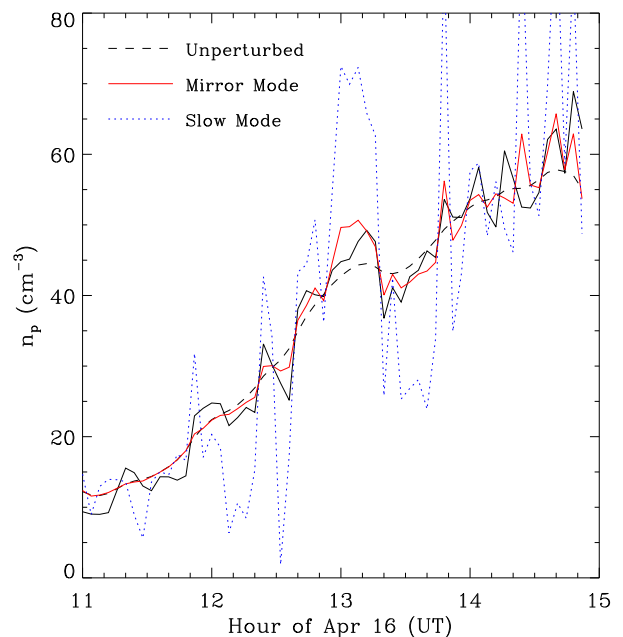
for the slow mode. Equations (3) and (5) can be used to compare data with theoretical predictions.

Figure 6 displays the density variations within a 4-hour interval in the sheath region. Note that the fluctuations seem to be periodic at later times. A frequency of  $1.04 \times 10^{-3}$  Hz stands out in the power spectrum of the fluctuations, which corresponds to a period of about 960 s. The smooth density profile is obtained by applying a Butterworth low-pass filter to the frequency space of the data and then converting it back to the time domain. We set the cutoff frequency of the filter to  $5 \times 10^{-4}$  Hz, smaller than the present wave frequency. The same filter is also applied to the magnetic field data to get the background field strength. The filter removes fluctuations with frequencies higher than the cutoff frequency, so the smoothed quantities represent the unperturbed profiles. Using these background quantities and the field variations, we obtain the density perturbations predicted by the mirror and slow modes from equations (3)

and (5), respectively. Figure 6 compares the observed and predicted density fluctuations. The density variations predicted by the mirror mode agree fairly well with observations after 12 UT on April 16; only one spike is missed at 14:17 UT. The slow mode also predicts the phase of the variation correctly, but gives much larger fluctuation amplitudes than observed. As implied by equation (3), the mirror mode density perturbation relative to the background is smaller in amplitude than the corresponding magnetic field variation for a moderate anisotropy, while the opposite is true across slow mode waves as described by equation (5). Stasiewicz [2004] reinterpreted the mirror mode fluctuations in the terrestrial magnetosheath as trains of slow mode solitons. In order to suppress the density variations, the author adopts  $\kappa = 0$ ,  $\gamma = 1.7$  for the relationship  $P_{\perp} \sim n^{\gamma} B^{\kappa}$ , whereas the CGL theory gives  $\kappa = 1$ ,  $\gamma = 1$  as required by the conservation of the magnetic moment. Therefore, we conclude that the wave activity is driven by the mirror mode. The density and magnetic field fluctuations in the PDL are significantly reduced (see Figure 3), probably due to the decrease in the plasma beta.

Note that the mirror mode is non-oscillatory and its proper treatment requires kinetic theory [e.g., Hasegawa, 1969; Southwood and Kivelson, 1993]. It arises as the result of the mirror instability which is a purely growing mode in a uniform plasma. The mirror mode may couple to propagating waves, for instance, the drift wave produced by magnetic field and density gradients [Hasegawa, 1969], and then convect away. The oscillatory structure in Figure 6 may result from this wave coupling. To illustrate this point, we write the dispersion relation as [Hasegawa, 1969]

$$\omega = \omega^* + i\xi\mu^{1/2} \left[ \eta - \left(1 + \frac{\mu}{\nu}\right) \frac{e^{\nu}}{I_0(\nu) - I_1(\nu)} \right], \quad (6)$$



**Figure 6.** Expanded view of the density fluctuations ahead of the PDL. Colored lines indicate density variations predicted by the slow and mirror modes, respectively. The background profile obtained from a low-pass filter is represented by the dashed line.

where

$$\begin{aligned}\xi &= \left(\frac{2}{\pi}\right)^{1/2} \left(\frac{T_{\parallel}}{T_{\perp}}\right)^{3/2} \frac{\Omega_p}{\beta_{\perp}}, \\ \eta &= \beta_{\perp} \left(\frac{T_{\perp}}{T_{\parallel}} - 1\right), \\ \mu &= \frac{k_{\parallel}^2}{\Omega_p^2} \frac{k_B T_{\perp}}{m_p}, \\ \nu &= \frac{k_{\perp}^2}{\Omega_p^2} \frac{k_B T_{\perp}}{m_p}.\end{aligned}$$

Here  $\omega^*$  is the frequency of the wave that the mirror mode is coupled to, and  $I_0, I_1$  are the modified Bessel functions of the first kind with order 0 and 1. Note that the electron contribution to this dispersion relation is factored out by assuming a cold electron distribution. Without the wave coupling, the wave frequency  $\omega$  is purely imaginary and as a result the mirror wave is non-propagating. This point contradicts the perspective of fluid theory. The onset condition expressed by equation (1) is derived from the above equation in the long wavelength limit when the perpendicular wave number  $k_{\perp}$  is much larger than the parallel wave number  $k_{\parallel}$ . Here we use equation (6) to estimate the maximum growth rate of the mirror instability. Shown by this equation, the growth rate is proportional to  $k_{\parallel}$ . While  $k_{\perp} \gg k_{\parallel}$ , the maximum growth rate will be restricted by the effect of finite Larmor radius since the perpendicular wavelength cannot be smaller than the ion Larmor radius. Taking derivatives of that equation with respect to  $\mu$  and  $\nu$  and equating them to zero, we obtain the maximum growth rate expressed as

$$\gamma_m = \left(\frac{3}{\pi}\right)^{1/2} \frac{1}{6\beta_{\perp}} \left(\frac{T_{\perp}}{T_{\parallel}}\right)^{-3/2} (\eta - 1)^2 \Omega_p \quad (7)$$

for  $k_{\parallel} \ll k_{\perp}$  in the long wavelength limit. Note that  $\eta$  is a measure of the overshoot of the mirror instability which must be larger than 1 as required by equation (1). The theoretical growth rate is displayed in Figure 7 over the two dimensional plane of the parallel plasma beta and thermal

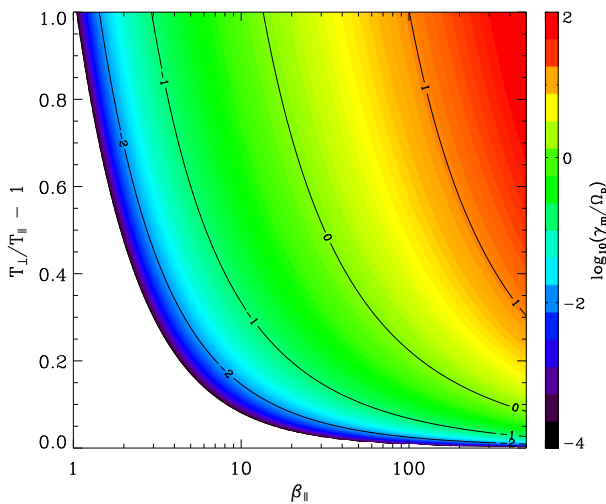


**Figure 7.** Theoretical growth rate of the mirror instability as a function of the parallel plasma beta and temperature anisotropy. The color bar indicates the logarithmic scale of the growth rate in units of the proton cyclotron frequency. Contour lines show the growth rate levels of  $[10^{-2}, 10^{-1}, 10^0, 10^1] \times \Omega_p$ .

anisotropy under the constraint of  $\eta > 1$ . As is evident from the figure, a significant growth rate occurs only in high beta regions when the thermal anisotropy is moderate. The best power law fit to the  $0.01\Omega_p$  level of the growth rate over the range  $5 \leq \beta_{\parallel p} \leq 50$  in the form of equation (2) gives  $S = 1.05$  and  $\alpha = 0.85$ , close to but lower than the numerical evaluation of Gary et al. [1997] in the same domain. In the current case, the average observed values  $\beta_{\perp p} \simeq 12$  and  $\frac{T_{\perp p}}{T_{\parallel p}} \simeq 1.2$  result in  $\gamma_m = 0.02\Omega_p$ , which seems reasonable for the overshoot of the instability of  $\eta \simeq 2.4$ .

## 4. Superposed Epoch Analysis

In the previous section, we presented an example showing the presence of a PDL and mirror mode waves in front of an MC. ICME data in the literature often show these features [e.g., Neugebauer and Goldstein, 1997, Figure 3; Bothmer and Schwenn, 1998, Figures 4, 5, 6, 7 and 8; Webb et al., 2000, Figure 6; Mulligan and Russell, 2001, Figures 1 and 2; Richardson et al., 2002, Figure 2; Richardson et al., 2004, Figure 1; Zurbuchen and Richardson, 2004, Figure 2; Gosling et al., 2005, Figure 1]; all these ICMEs are preceded by shocks. In this section, we use a superposed epoch analysis (SEA) to give a broad-based view of these features. We define the ICME arrival time as the zero epoch and superpose the ICME-related data for the three ICME classes (MCs with shocks, non-MC ICMEs with shocks, ICMEs without shocks) separately. Typical uncertainties in identifying the beginning of an ICME are estimated to be 1 - 2 hours depending on the time resolution of the data. ICMEs with preceding shocks are scaled into a 30 hour long interval (the average duration of an ICME at 1 AU) and the sheath regions are scaled into 14 hour intervals (the average duration of the sheath at 1 AU); ICMEs without shocks are scaled into the same interval, but since there is no sheath region we use the 14 hours of data ahead of the ICMEs. Thus we line up the data in a fixed time relation to the ICME arrival times as if we had many observations of a single event. By averaging the superposed data for each time, real signals will be preserved but noise will tend to average out [e.g., Haurwitz and Brier, 1981; Prager and Hoenig, 1989].

Figure 8 displays the superposed 4 m averages of ACE plasma and magnetic data for the three categories of ICMEs. As required by our ICME identification criteria, the ICME intervals (the data after the zero epoch) have a depressed proton temperature and the MCs (left panels) possess a strong magnetic field. The first two classes of ICMEs have expansion speeds (the speed difference between the leading and trailing edges) of about  $90 \text{ km s}^{-1}$ ; the third class of ICMEs, those without preceding shocks, has an expansion speed of about  $20 \text{ km s}^{-1}$ . As a result of this expansion, the first two ICME classes have a lower average plasma density than the third class. Using the ambient solar wind density  $n = 6.5 \text{ cm}^{-3}$ , temperature  $T = 10^5 \text{ K}$  and magnetic field strength  $B = 7 \text{ nT}$  derived from the data ahead of the ICMEs in the right panels, we estimate the fast mode speed from  $v_f = (v_A^2 + \frac{5k_B T}{3m_p})^{1/2}$  to be around  $70 \text{ km s}^{-1}$ . The expansion speed can be regarded as the ICME speed relative to the ambient solar wind, which is larger than the fast mode speed for the first two ICME classes. Consequently, shock waves should be driven ahead of the fast ICMEs, consistent with the data in Figure 8. For all ICMEs, the expansion speed is of order of the Alfvén speed,  $50 - 60 \text{ km s}^{-1}$  at 1 AU. This result is in agreement with previous findings [e.g., Burlaga et al., 1981; Liu et al., 2005].

In the left and middle panels, the superposed shock occurs 14 hours before the arrival time of the ICMEs; between the shock and the ICME is the sheath region where PDLs and mirror mode waves may occur. For MCs with preceding

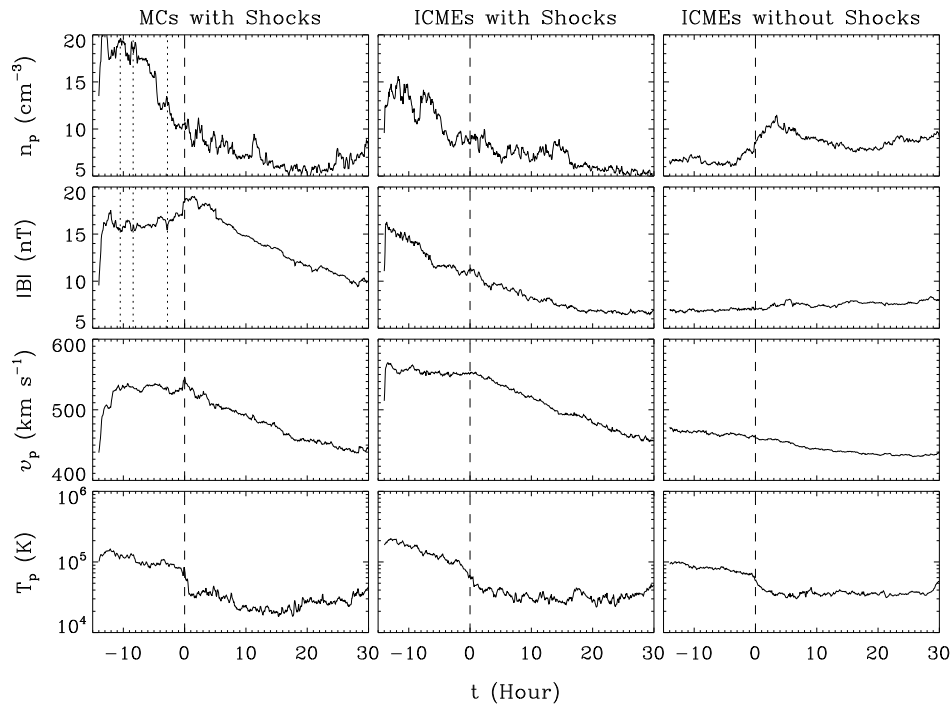


**Figure 8.** Superposed epoch plots of the proton density, magnetic field strength, bulk speed and proton temperature for the three classes of ICMEs. The zero time (dashed lines) is the ICME forward boundary. Dotted lines align some magnetic field dips with the corresponding density spikes in the MC sheath.

shocks (left panels), a PDL is present beginning about six hours ahead of the ICME in which the proton density decreases by a factor of about 1.7 and the field magnitude gradually increases. The anti-correlated density and magnetic field fluctuations, with some times marked by the dotted lines, show that wave structures are also present. Presumably these structures are induced by the mirror instability; the superposed thermal anisotropy supports this interpretation (see Figure 9). Plasma depletion may also occur in the sheath region of ICMEs with shocks (middle panels). The plasma is rarefied in the layer adjacent to these ICMEs, but the magnetic field magnitude remains roughly constant. The density and magnetic field have high-frequency fluctuations, but no coherent structure is apparent. The sheath regions of the first two ICME classes thus show a different association with the PDL and mirror waves, which may reveal the dependence of these features on the ICME geometry. MCs are better organized than common ICMEs in terms of magnetic structure and may lead to favorable conditions for such features to develop. The ICMEs not associated with shocks (right panels) do not have PDLs and the density and magnetic fluctuations are even further reduced. The compression of the ambient solar wind by these ICMEs is apparently not large enough to produce these features, contrary to the suggestion of Farrugia et al. [1997] that a PDL may form irrespective of whether ICMEs drive shocks or not. Figure 8 indicates that shocks may be necessary to produce these features, since their formation is closely related to the extent of the compression. Observations of PDLs in planetary magnetosheaths show a gradual increase in the magnetic field simultaneous with the density decrease [e.g., Crooker et al., 1979; Hammond et al., 1993; Violante et al., 1995]. This increase in the field strength may not be required in ICME sheaths. The upstream field compression by ICMEs may be alleviated by the sheath expansion as the preceding shocks move away from the ejecta.

The speed and field strength profiles within ICMEs are smooth compared with the turbulent profiles of the density and temperature. As is well known, Alfvén waves give rise

to correlated velocity and magnetic field fluctuations [e.g., Stix, 1962]. The low-frequency Alfvén waves may be responsible for solar wind heating and acceleration through a non-linear cascade process of energy [e.g., Isenberg and Hollweg, 1983; Goldstein et al., 1995; Leamon et al., 1999; Hu and Habbal, 1999]. Radial evolution of ICMEs is investigated by Liu et al. [2006]; they find that the ICME temperature decreases more slowly with distance than an adiabatic profile. This plasma heating may not be powered by Alfvén waves since they are not prevalent within ICMEs as implied by the smooth speed and magnetic field profiles.

Mirror waves can also be evidenced by the temperature anisotropy. Figure 9 shows the superposed thermal anisotropy data from Wind for the three classes of ICMEs. The threshold instability conditions, calculated from the superposed parallel plasma beta  $\beta_{\parallel p}$  using equation (2), are plotted to allow comparison with the anisotropy. An abrupt increase in the mirror and cyclotron thresholds can be seen at the leading edge of the first two groups of ICMEs (left and middle panels); it is stronger in the first case, indicating that the plasma beta is low within these MCs. For the third ICME class (right panel), the onset conditions inside and outside the ICMEs are similar. The ICME plasma typically has an anisotropy near zero, so it is stable with respect to temperature anisotropy instabilities. This point is consistent with the picture described by Figure 2. The thermal anisotropy increases to 0.1 - 0.4 in the sheath regions of the first ICME category (left panel) and is very close to the instability thresholds at some epochs. The sheath plasma may be marginally unstable to the mirror and cyclotron instabilities. As a result, mirror waves may be induced under certain conditions and then be carried away by coupling to other propagating modes. This interpretation is in accord with the anti-correlated density and magnetic field fluctuations seen in Figure 8 (left panels). The temperature anisotropy may also be enhanced in the sheaths of the second ICME class (middle panel), but not as strongly, so the fluctuations

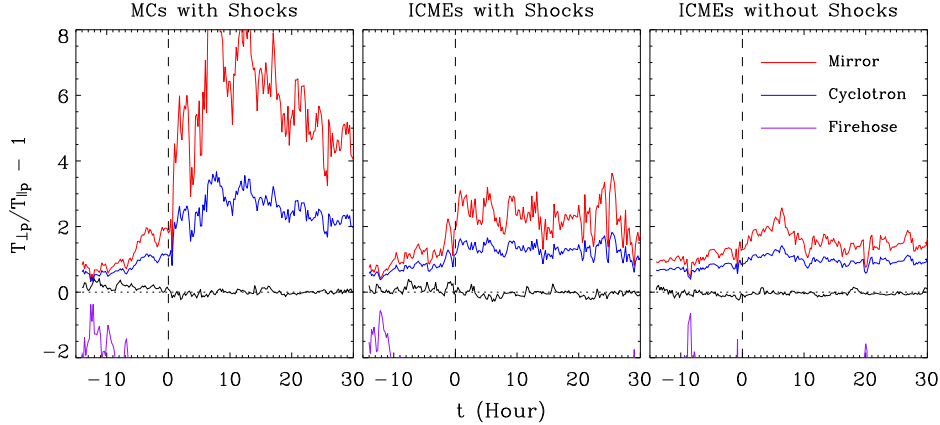


**Figure 9.** Superposed epoch plots of proton thermal anisotropy for the same three classes of ICMEs as in Figure 8. Dashed lines mark the ICME arrival times while dotted lines show the zero level of the anisotropy. Threshold conditions for the instabilities are represented by the colored lines.

are reduced as shown in Figure 8 (middle panels). For the third ICME group (right panel), the thermal anisotropy does not deviate from zero across the sheath and ICME intervals, so mirror waves do not appear.

The superposed parallel proton beta  $\beta_{\parallel p}$  ranges from 0.5 to 5.5 in the sheath regions of the MCs with preceding shocks. In this regime, the instabilities are dominated by the cyclotron mode since it has a lower threshold than the mirror mode (refer to Figure 2). Gary [1992] showed through numerical evaluation of the Vlasov dispersion relation that the cyclotron instability has a higher linear growth rate. The temperature anisotropy can be rapidly reduced by the cyclotron instability and thus the mirror mode may not develop to a significant level. However, Price et al. [1986] found that the introduction of a small fraction of minor ions would substantially lower the growth rate of the cyclotron instability while leaving the mirror mode unaffected. Since helium ions are always present in the solar wind, the mirror mode would be able to grow given the observed plasma beta and thermal anisotropy.

It should be noted that the SEA smoothes the data. Consequently, the superposed field magnitude and density do not exhibit large fluctuations. The smoothed profiles of the threshold conditions and thermal anisotropy also underestimate the marginal instability to the mirror mode. Examining ICMEs individually is the best way to see the mirror mode structures, as demonstrated by the case study in section 3. The references listed in the first paragraph of section 4 give ICMEs that often show the mirror mode fluctuations (and PDLs) in their sheath regions; large dips in the magnetic field strength serve as a good identifier for the mirror mode structures.

## 5. Conclusions and Discussion

In analogy with planetary magnetosheaths, we propose that PDLs and mirror mode structures form in the sheath regions of fast ICMEs. The upstream field compression by fast ICMEs and their leading shocks results in field line draping and anisotropic plasma heating in the sheath. An extensive case study and statistical analysis of ICMEs observed by ACE and Wind show that these two features occur in the sheaths ahead of fast events.

The association of plasma depletion and mirror waves with ICMEs is demonstrated by an MC example observed at ACE and Wind on 16 April 1999. This event drives a forward oblique shock with its axis perpendicular to the shock normal. Downstream of the shock, the proton density decreases by a factor of 2 within 2.6 hours (corresponding to

0.03 AU in length) ahead of the MC. At the same time the magnetic field is stretched to be nearly radial and normal to the MC axis. Anti-correlated density and field strength fluctuations are seen inside the sheath region between the MC and the shock and are consistent with mirror mode waves; the thermal anisotropy exceeds the mirror mode onset condition and the plasma beta is high. Analytical growth rates of the mirror instability limited by the effect of finite Larmor radius are obtained as a function of plasma beta and temperature anisotropy. From the observed overshoot of the mirror instability the maximum growth rate is estimated to be around  $0.02\Omega_p$ .

We perform a SEA on three classes of ICMEs to investigate the general properties of PDLs and mirror mode waves associated with these different kinds of events. On average, the sheath region is about 14 hours long (roughly 0.17 AU) at 1 AU in comparison with the 0.2 - 0.3 AU span of ICME intervals. For MCs preceded by shocks, PDLs are observed to have an average density decrease of a factor of 1.7 which lasts about 6 hours and is accompanied by a gradual increase in the field magnitude. The average thermal anisotropy  $\frac{T_{\perp p}}{T_{\parallel p}} \simeq 1.2 - 1.3$ , close to the threshold for the mirror instability, leads to anti-correlated fluctuations in the density and magnetic field strength. Compared with the MCs, non-MC ICMEs with forward shocks have a thinner plasma depletion layer close to their leading edges. The thermal anisotropy is only slightly enhanced, so fluctuations in the density and magnetic field are smaller and do not have a definite structure. This difference between the two classes may indicate the effect of the ICME geometry in creating the features. The third category, ICMEs without shocks, is not associated with plasma depletion and mirror waves. The occurrence of these signatures may be determined by the extent of the upstream field compression by ICMEs. As a measure of the compression, an ICME speed of about 90 km s<sup>-1</sup> relative to the ambient solar wind seems necessary to drive shocks and produce the features. As revealed by the SEA, all the ICME plasma is stable to the temperature anisotropy instabilities, consistent with the finding of Liu et al. [2006].

These results reveal important physical processes which alter the ICME environment and provide another setting in which to study PDLs and mirror mode waves. As noted by Zwan and Wolf [1976], PDLs can only develop in the absence of significant magnetic reconnection; otherwise, flux tubes that are compressed against the magnetosphere would merge with geomagnetic field lines before they are diverted



around the obstacle. The same condition should hold in ICME sheaths for the squeezing process to be operative. An ideal MHD simulation of plasma flow behind MC-driven shocks also seems to confirm that the PDL becomes thinner with a small increase in the reconnection rate [Erkaev et al., 1995]. McComas et al. [1988; 1994] suggest that magnetic reconnection should commonly take place between fast ICMEs and the upstream ambient solar wind in the same manner as occurs at the dayside of the magnetopause. Direct evidence for the local reconnection in the solar wind was not provided until recently, but none of the reconnection sites are at the interface between ICMEs and the upstream solar wind [Gosling et al., 2005]. Given the frequency of PDLs in ICME sheaths, magnetic reconnection may not be prevalent or locally important in the sheath regions of fast ICMEs.

Observations of planetary magnetosheaths indicate that mirror waves can make large depressions, i.e., holes in the background magnetic field [e.g., Kaufmann, et al., 1970; Tsurutani et al., 1992; Violante et al., 1995]. This point is emphasized by Winterhalter et al. [1994] who made a survey of magnetic holes observed at Ulysses and examined their relationship with mirror instabilities. Consistent with the results of Klein and Burlaga [1980], they find that the holes tend to occur in the interaction regions where fast streams overtake the ambient solar wind and the mirror mode is marginally stable. Non-linear saturation mechanisms of the mirror instability are qualitatively discussed by Kivelson and Southwood [1996]. In the non-linear saturation process, marginal stability can be achieved by large reductions in the magnetic field, so the fully evolved state would be characterized by holes in the background magnetic field rather than alternate field enhancements and depressions. However, Bavassano Cattaneo et al. [1998] suggest that mirror waves make field enhancements as well as dips based on Voyager observations of Saturn's magnetosheath. According to Figure 7, the mirror instability will grow quickly and consequently make a series of holes when the plasma beta is high; adjacent holes are so close that the magnetic field appears to be alternately enhanced and depressed. When the plasma beta is occasionally high, the hole will be isolated. Their observed plasma beta profile seems to support this explanation. If the interpretation that magnetic holes are remnants of mirror mode structures is correct, the mechanism suggested here would be able to explain the creation of some magnetic holes localized in the solar wind in a self-consistent manner.

Mirror waves may contribute to energetic particle modulation and acceleration in the sheath regions of ICMEs. Various studies of the cosmic ray modulation in the solar wind show that enhanced magnetic turbulence in the sheath is particularly effective in producing Forbush decreases [e.g., Badruddin et al., 1991; Ifedili, 2004], probably due to particle scattering by waves or their non-linear evolved states. According to Kivelson and Southwood [1996], the final evolved state of mirror waves would be such that the total perpendicular pressure (plasma plus field) is constant along the field line. Particles with small pitch angles will be constrained by the mirror force  $F = -\mu\nabla_{\parallel}B$ , where  $\mu$  is the magnetic moment; if the magnetic moment and total energy are invariant, motion of these particles into weak field regions along the field line will convert perpendicular energy to parallel and kinetic energy, which can serve to suppress growth of the mirror instability. Particles with large pitch angles may be excluded from strong field regions, also leading to the pressure balance.

## Appendix A: Test of Superposed Epoch Analysis

Superposed epoch analysis (SEA) is useful to identify the association of individual features with key events (here defined as the ICME arrival times) in time series data. The statistical significance of the association can be determined

by a randomization technique which avoids the assumptions of normality, random sampling and sample independence made by parametric testing [e.g., Haurwitz and Brier, 1981; Prager and Hoenig, 1989]. The null hypothesis is that plasma depletion and mirror waves are not associated with ICMEs. Under this null hypothesis, any time in the data can be considered as a key event, i.e., an ICME arrival time.

We use the 4 m averages of ACE proton density data from 1998 - 2005 as a proxy for the significance test. We repeatedly draw random sets of locations for the key event and their corresponding background times from the data. Key events closer than a minimum spacing of 27 days are discarded to avoid the effect of solar sector crossings. Each randomization yields 39 positions of simulated ICME arrival times and 660 background spectra corresponding to each key event (210 before and 450 after). For each set, we compute the t-statistic defined as

$$t = \frac{\bar{E} - \bar{B}}{\sqrt{\frac{(m+n)(\sigma_E^2 + n\sigma_B^2)}{mn(m+n-2)}}},$$

where  $\sigma_E$  and  $\sigma_B$  are the standard deviations of the  $m = 39$  key events and  $n = 660 \times 39$  background times respectively, and  $\bar{E}$ ,  $\bar{B}$  are their corresponding means. This statistic obeys Student's t-distribution with degrees of freedom  $m + n - 2$  for normally distributed and independent data. The observed t-statistic is calculated from the true arrival times of the 39 ICMEs with preceding shocks used in our analysis. The frequency distribution of the simulated t-statistic resulting from 10,000 runs of the randomization is displayed in Figure 10 as a histogram with a bin size of 0.1. Compared with the Gaussian fit, the distribution skews toward the high-value tail. The significance level can be estimated from the relative frequency with which the simulated t-statistic is smaller than or equal to the observed one. The observed statistic is about 0.91, corresponding to a significance level of 91%. In contrast, the standard t-distribution gives 82% for the observed statistic.

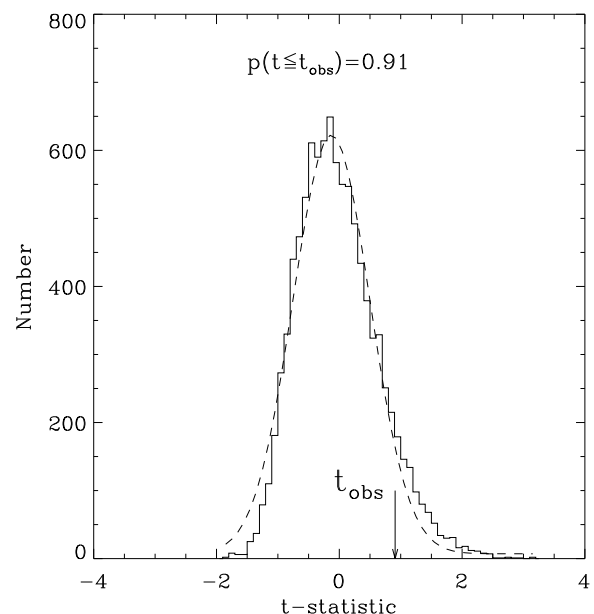


**Figure 10.** Histogram distribution of the t-statistic from the Monte Carlo simulations with its Gaussian fit denoted by the dashed line. The arrow indicates the value of the real statistic while the upper text shows the significance level.

**Acknowledgments.** We acknowledge the use of the magnetic field data of ACE and Wind from the NSSDC. The work at MIT was supported under NASA contract 959203 from JPL to MIT, NASA grants NAG5-11623 and NNG05GB44G, and by NSF grants ATM-0203723 and ATM-0207775.

## References

- Badruddin, Mr., D. Venkatesan, and B. Y. Zhu (1991), Study and effect of magnetic clouds on the transient modulation of cosmic-ray intensity, *Solar Phys.*, *134*, 203.
- Bavassano Cattaneo, M. B., C. Basile, G. Moreno, and J. D. Richardson (1998), Evolution of mirror structures in the magnetosheath of Saturn from the bow shock to the magnetopause, *J. Geophys. Res.*, *103*, 11,961.
- Bothmer, V., and R. Schwenn (1998), The structure and origin of magnetic clouds in the solar wind, *Ann. Geophys.*, *16*, 1.
- Burlaga, L., E. Sittler, F. Mariani, and R. Schwenn (1981), Magnetic loop behind an interplanetary shock: Voyager, Helios, and IMP 8 observations, *J. Geophys. Res.*, *86*, 6673.
- Chandrasekhar, S. A., A. N. Kaufman, and K. M. Watson (1958), The stability of the pinch, *Proc. Roy. Soc. London, Ser. A*, *245*, 435.
- Chew, G. F., M. L. Goldberger, and F. E. Low (1956), The Boltzmann equation and the one-fluid hydromagnetic equations in the absence of particle collisions, *Proc. Roy. Soc. London, Ser. A*, *236*, 112.
- Crooker, N. U., and G. L. Siscoe (1977), A mechanism for pressure anisotropy and mirror instability in the dayside magnetosheath, *J. Geophys. Res.*, *82*, 185.
- Crooker, N. U., T. E. Eastman, and G. S. Stiles (1979), Observations of plasma depletion in the magnetosheath at the dayside magnetopause, *J. Geophys. Res.*, *84*, 869.
- Erkaev, N. V., C. J. Farrugia, H. K. Biernat, L. F. Burlaga, and G. A. Bachmaier (1995), Ideal MHD flow behind interplanetary shocks driven by magnetic clouds, *J. Geophys. Res.*, *100*, 19,919.
- Farrugia, C. J., N. V. Erkaev, H. K. Biernat, L. F. Burlaga, R. P. Lepping, and V. A. Osherovich (1997), Possible plasma depletion layer ahead of an interplanetary ejecta, *J. Geophys. Res.*, *102*, 7087.
- Gary, S. P. (1992), The mirror and the ion cyclotron anisotropy instabilities, *J. Geophys. Res.*, *97*, 8519.
- Gary, S. P., J. Wang, D. Winske, and S. A. Fuselier (1997), Proton temperature anisotropy upper bound, *J. Geophys. Res.*, *102*, 27,159.
- Gary, S. P., R. M. Skoug, J. T. Steinberg, and C. W. Smith (2001), Proton temperature anisotropy constraint in the solar wind: ACE observations, *Geophys. Res. Lett.*, *28*, 2759.
- Goldstein, M. L., D. A. Roberts, and W. H. Matthaeus (1995), Magnetohydrodynamic turbulence in the solar wind, *Ann. Rev. Astron. Astrophys.*, *33*, 283.
- Gosling, J. T., and D. J. McComas (1987), Field line draping about fast coronal mass ejecta: A source of strong out-of-ecliptic interplanetary magnetic fields, *Geophys. Res. Lett.*, *14*, 355.
- Gosling, J. T., R. M. Skoug, D. J. McComas, and C. W. Smith (2005), Direct evidence for magnetic reconnection in the solar wind near 1 AU, *J. Geophys. Res.*, *110*, A01107, doi:10.1029/2004JA010809.
- Hammond, C. M., J. L. Phillips, S. J. Bame, E. J. Smith, and C. G. MacLennan (1993), Ulysses observations of the planetary depletion layer at Jupiter, *Plan. Space Sci.*, *41*, 857.
- Hasegawa, A. (1969), Drift mirror instability in the magnetosphere, *Phys. Fluids*, *12*, 2642.
- Hau, L.-N., and B. U. Ö. Sonnerup (1999), Two-dimensional coherent structures in the magnetopause: Recovery of static equilibria from single-spacecraft data, *J. Geophys. Res.*, *104*, 6899.
- Haurwitz, M. W., and G. W. Brier (1981), A critique of the superposed epoch analysis method: Its application to solar-weather relations, *Mon. Wea. Rev.*, *109*, 2074.
- Hill, P., G. Paschmann, R. A. Treumann, W. Baumjohann, N. Skopke, and H. Lühr (1995), Plasma and magnetic field behavior across the magnetosheath near local noon, *J. Geophys. Res.*, *100*, 9575.
- Hu, Q., and B. U. Ö. Sonnerup (2002), Reconstruction of magnetic clouds in the solar wind: Orientations and configurations, *J. Geophys. Res.*, *107*, 1142, doi:10.1029/2001JA000293.
- Hu, Y.-Q., and S. R. Habbal (1999), Resonant acceleration and heating of solar wind ions by dispersive ion cyclotron waves, *J. Geophys. Res.*, *104*, 17,045.
- Ifedili, S. O. (2004), The two-step Forbush decrease: An empirical model, *J. Geophys. Res.*, *109*, A02117, doi:10.1029/2002JA009814.
- Isenberg, P. A., and J. V. Hollweg (1983), On the preferential acceleration and heating of solar wind heavy ions, *J. Geophys. Res.*, *88*, 3923.
- Kasper, J. C., A. J. Lazarus, and S. P. Gary (2002), Wind/SWE observations of firehose constraint on solar wind proton temperature anisotropy, *Geophys. Res. Lett.*, *29*, 1839, doi:10.1029/2002GL015128.
- Kaufmann, R. L., J.-T. Horng, and A. Wolfe (1970), Large-amplitude hydrodynamic waves in the inner magnetosheath, *J. Geophys. Res.*, *75*, 4666.
- Kivelson, M. G., and D. J. Southwood (1996), Mirror instability II: The mechanism of nonlinear saturation, *J. Geophys. Res.*, *101*, 17,365.
- Klein, L., and L. F. Burlaga (1980), Interplanetary sector boundaries 1971 - 1973, *J. Geophys. Res.*, *85*, 2269.
- Leamon, R. J., C. W. Smith, N. F. Ness, and H. K. Wong (1999), Dissipation range dynamics: Kinetic Alfvén waves and the importance of  $\beta_e$ , *J. Geophys. Res.*, *104*, 22,331.
- Lepping, R. P., J. A. Jones, and L. F. Burlaga (1990), Magnetic field structure of interplanetary magnetic clouds at 1 AU, *J. Geophys. Res.*, *95*, 11,957.
- Liu, Y., J. D. Richardson, and J. W. Belcher (2005), A statistical study of the properties of interplanetary coronal mass ejections from 0.3 to 5.4 AU, *Plan. Space Sci.*, *53*, 3, doi:10.1016/j.pss.2004.09.023.
- Liu, Y., J. D. Richardson, J. W. Belcher, J. C. Kasper, and H. A. Elliott (2006), Thermodynamic structure of collision-dominated expanding plasma: Heating of interplanetary coronal mass ejections, *J. Geophys. Res.*, *111*, A01102, doi:10.1029/2005JA011329.
- Lopez, R. E. (1987), Solar cycle invariance in solar wind proton temperature relationships, *J. Geophys. Res.*, *92*, 11,189.
- McComas, D. J., J. T. Gosling, D. Winterhalter, and E. J. Smith (1988), Interplanetary magnetic field draping about fast coronal mass ejecta in the outer heliosphere, *J. Geophys. Res.*, *93*, 2519.
- McComas, D. J., J. T. Gosling, C. M. Hammond, M. B. Moldwin, J. L. Phillips, and R. J. Forsyth (1994), Magnetic reconnection ahead of a coronal mass ejection, *Geophys. Res. Lett.*, *21*, 1751.
- Mulligan, T., and C. T. Russell (2001), Multispacecraft modeling of the flux rope structure of interplanetary coronal mass ejections: Cylindrically symmetric versus nonsymmetric topologies, *J. Geophys. Res.*, *106*, 10,581.
- Neugebauer, M., and R. Goldstein (1997), Particle and field signatures of coronal mass ejections in the solar wind, in *Coronal Mass Ejections, Geophys. Monogr. Ser.*, vol. 99, edited by N. Crooker, J. A. Joselyn and J. Feynman, pp. 245, AGU, Washington, D.C.
- Parker, E. N. (1958), Dynamical instability in an anisotropic ionized gas of low density, *Phys. Rev.*, *109*, 1874.
- Parks, G. K. (Ed.) (2004), *Physics of Space Plasmas - An Introduction*, 2nd ed., Westview Press, Boulder.
- Prager, M. H., and J. M. Hoenig (1989), Superposed epoch analysis: A randomization test of environmental effects on recruitment with application to chub Mackerel, *Trans. Amer. Fish. Soc.*, *118*, 608.
- Price, C. P., D. W. Swift, and L. C. Lee (1986), Numerical simulation of nonoscillatory mirror waves at the Earth's magnetosheath, *J. Geophys. Res.*, *91*, 101.
- Richardson, J. D., K. I. Paularena, C. Wang, and L. F. Burlaga (2002), The life of a CME and the development of a MIR: From the Sun to 58 AU, *J. Geophys. Res.*, *107*, 1041, doi:10.1029/2001JA000175.
- Richardson, J. D., Y. Liu, and J. W. Belcher (2004), Propagation and evolution of ICMES in the solar wind, in *Multiscale Processes in the Earth's Magnetosphere: From Interball to Cluster, NATO Science Series II: Mathematics, Physics and Chemistry*, vol. 178, edited by J.-A. Sauvaud and Z. Němeček, pp. 1, Kluwer Academic Publishers, Netherlands.

- Sonnerup, B. U. Ö, and L. J. Cahill, Jr. (1967), Magnetopause structure and attitude from Explorer 12 observations, *J. Geophys. Res.*, *72*, 171.
- Southwood, D. J., and Kivelson M. G. (1993), Mirror instability: 1. Physical mechanism of linear instability, *J. Geophys. Res.*, *98*, 9181.
- Stasiewicz, K. (2004), Reinterpretation of mirror modes as trains of slow magnetosonic solitons, *Geophys. Res. Lett.*, *31*, L21804, doi:10.1029/2004GL021282.
- Stix, T. H. (Ed.) (1962), *The Theory of Plasma Waves*, McGraw-Hill, New York.
- Tsurutani, B. T., D. J. Southwood, E. J. Smith, and A. Balogh (1992), Nonlinear magnetosonic waves and mirror mode structures in the March 1991 Ulysses interplanetary event, *Geophys. Res. Lett.*, *19*, 1267.
- Viñas, A. F., and J. D. Scudder (1986), Fast and optimal solution to the 'Rankine-Hugoniot problem', *J. Geophys. Res.*, *91*, 39.
- Violante, L., M. B. Bavassano Cattaneo, G. Moreno, and J. D. Richardson (1995), Observations of mirror waves and plasma depletion layer upstream of Saturn's magnetopause, *J. Geophys. Res.*, *100*, 12,047.
- Webb, D. F., E. W. Cliver, N. U. Crooker, O. C. St. Cry, and B. J. Thompson (2000), Relationship of halo coronal mass ejections, magnetic clouds, and magnetic storms, *J. Geophys. Res.*, *105*, 7491.
- Winterhalter, D., M. Neugebauer, B. E. Goldstein, E. J. Smith, S. J. Bame, and A. Balogh (1994), Ulysses field and plasma observations of magnetic holes in the solar wind and their relation to mirror-mode structures, *J. Geophys. Res.*, *99*, 23,371.
- Zurbuchen, T. H., and I. Richardson (2004), In-situ solar wind and magnetic field signatures of interplanetary coronal mass ejections, *Space Sci. Rev.*, in press.
- Zwan, B. J., and R. A. Wolf (1976), Depletion of solar wind plasma near a planetary boundary, *J. Geophys. Res.*, *81*, 1636.
- 
- Y. Liu, Kavli Institute for Astrophysics and Space Research, Massachusetts Institute of Technology, Room 37-676a, Cambridge, MA 02139, USA. (liuxying@space.mit.edu)